Three dimensional aerodynamic optimization for an ultra-low aspect ratio transonic turbine stator blade

Martina Hasenjäger, Bernhard Sendhoff, Toyotaka Sonoda, Toshiyuki Arima

2005

GT2005-68680

THREE DIMENSIONAL AERODYNAMIC OPTIMIZATION FOR AN ULTRA-LOW ASPECT RATIO TRANSONIC TURBINE STATOR BLADE

Martina Hasenjäger[1], **Bernhard Sendhoff**[1], **Toyotaka Sonoda**[2], **Toshiyuki Arima**[3]
[1] Honda Research Institute Europe GmbH
Carl-Legien-Str. 30, D-63073 Offenbach/Main, Germany

[2] Wako Nishi R&D Center, Honda R&D Ltd.
1-4-1 Chuo, Wako-shi, Saitama 351-0193, Japan

[3] Wako Research Center, Honda R&D Ltd.
1-4-1 Chuo, Wako-shi, Saitama 351-0193, Japan

ABSTRACT

A modern numerical stochastic optimization method, namely the evolution strategy (ES), was applied to an ultra-low aspect ratio transonic turbine stator blade in order to seek a new aerodynamic design concept for lower secondary flow losses. The low stator blade count is selected to avoid the direct viscous interaction of the stator wake with the downstream rotor blade. This led to the ultra-low aspect ratio stator blade. In the optimization, two kinds of objective functions were used, that is, (1) minimization of the "aerodynamic loss" (a single objective), (2) minimization of the "aerodynamic loss" and of the "variation of circumferential static pressure distribution" downstream of the stator blade (multi-objective optimization). In the case of the single objective, the aerodynamic loss is improved by an extreme aft-loaded airfoil with a noticeable bent part near the trailing edge, although the circumferential static distribution is slightly worse than that of the baseline. In the case of the multi-objective optimization, we observe a trade-off relation between aerodynamic loss and variation of static pressure distribution which is not easily resolved. A new design concept to achieve lower aerodynamic loss for ultra-low aspect ratio transonic turbine stator blades is discussed.

NOMENCLATURE

β_2	exit flow angle
$\delta\beta_2$	tolerance in exit flow angle
C	chord length
M	Mach number
ω	total pressure loss $= 1 - \frac{Pt_2}{Pt_1}$
Pt	total pressure
Ps	static pressure
PST	static outlet pressure
PST_{VAR}	pitch-wise variation of the static outlet pressure
Θ_{min}	minimum thickness of the blade
Θ_{max}	maximum thickness of the blade
$\Theta_{TE,min}$	minimum trailing edge thickness of the blade
$r\theta$	pitch-wise length
s	solidity
x	coordinate related to blade geometry (see Figs. 7 and 8)
X	coordinate related to stator passage and axial positions of cross-sectional blade to blade views (see Figs. 3, 11 and 12)
y^+	normal distance from wall in wall coordinate system

ABBREVIATIONS

AR   aspect ratio
NB   number of blades
LE   leading edge
TE   trailing edge
SS   suction side
PS   pressure side

SUBSCRIPTS

1   upstream position
2   just downstream stator TE or rotor LE position
3   far downstream of stator
ax   axial

INTRODUCTION

In general, low-aspect-ratio (low AR) turbine stator blades have rarely been adopted as components of conventional turbines because of their poor performance. This is caused primarily by increases of secondary flow losses due to the low AR. Therefore, the secondary flow phenomena have received much attention in the literature. It is known from experiments with low AR blades that the secondary flow loss is particularly increased near the hub-end-wall region [1]. Furthermore, for the commonly used one-dimensional loss model, the secondary flow loss is almost proportional to the AR [2–4].

A unique single-stage high pressure turbine has been recently developed that is characterized by ultra low-AR (span height / axial chord = 0.30) blades with the following design philosophy: "avoid a direct viscous interaction of the stator wake with the downstream rotor blade" [5]. The three dimensional outline of the blades and the flow fields based on CFD results are shown in Fig. 1. There is a very strong inward-radial cross flow on the suction side as compared to conventional high-AR blades (not shown here). The flow field near the hub-end-wall is very complicated due to the interaction of the secondary flow with the transonic main flow. As a result, the loss near the hub region is considerably increased as compared to conventional high-AR blades, as shown in Fig. 2. We can assume that the higher loss near the hub region leads to poor stage efficiency. Indeed, the stage efficiency is experimentally demonstrated to be only about 88% [5]; a value which is below the efficiency reached by state of the art high-AR turbines that reach values well above 90%.

It is unlikely that the advanced design principles for high AR blades will help us to improve the efficiency of ultra low-AR turbine stator blades. The flow phenomena that can be observed are too different to exploit design principles for high AR blades directly.

Therefore, the objective of this research is to find a new aerodynamic design concept for suppressing the secondary flow loss,
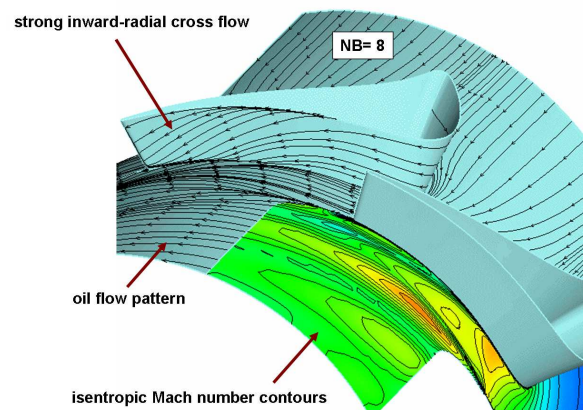

Figure 1. Ultra low aspect ratio turbine stator blades and their flow fields.
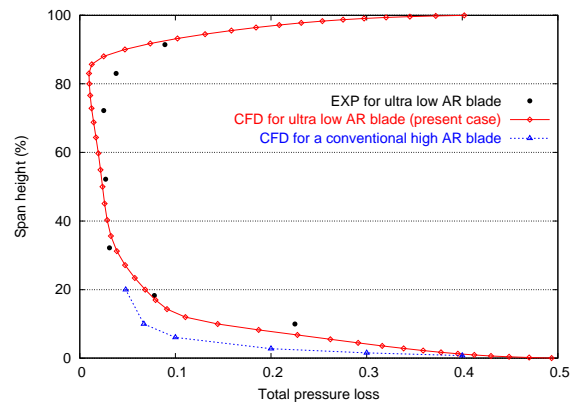

Figure 2. Radial total pressure loss distribution at stator exit (station 2) for ultra-low AR and conventional high-AR blades. Data are taken from [5].

focusing on the hub-end-wall region using numerical optimization methods.

Such a new design concept is likely to be useful also for the aerodynamic design of smaller gas turbine engines in general. The reason is that in both cases the key is to identify an aerodynamic design concept that is able to control the strong secondary flow, or in other words, the complicated three-dimensional nature of the flow.

Recently, many reports on numerical optimization methods have been published. For example, regarding the turbine components, design concepts of shock loss reduction in 2-D transonic turbine cascades [6], 3-D optimization for a high-lift turbine vane [7] and for a 1.5-stage turbine [8] have been reported. None of these optimizations deal with ultra low-AR blades.

ULTRA-LOW-AR TRANSONIC STATOR BLADES

Figure 3 shows the meridional passage of the ultra low-AR transonic turbine stator blades. The corrected mass flow rate is 0.87 kg/s with a zero inlet flow angle. The exit Mach number
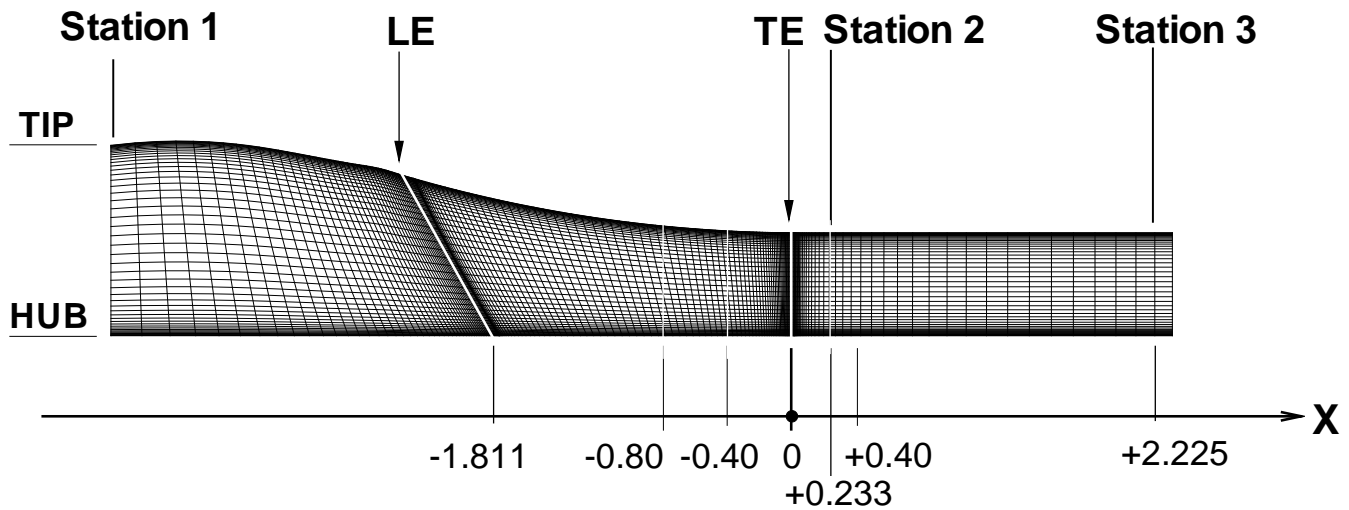
Figure 3.   Meridional passage for ultra-low aspect ratio stator blades.

and flow angle is 1.04 and 72.8 degrees at mid-span height, respectively. The blade count NB is only NB = 8. Due to manufacturing constraints, the blade geometry is defined by only two cross-sections, the hub and the tip section. Linear interpolation between these two sections is used to define the remaining blade geometry. The stator blade is circumferentially leaned by 14 degrees in order to suppress the development of secondary flow near the hub-end-wall.

Coordinate $X = 0$ corresponds to the trailing edge (TE) of the ultra-low-AR blade and $X = 0.233$ refers to the LE-location downstream of the rotor blade, called *station 2*. For additional information on the design specifications of the ultra-low AR blade the reader is referred to [5]. In the following, we will refer to this blade as the *baseline blade*, in particular when we compare it to the optimization results.

DESIGN OPTIMIZATION WITH EVOLUTIONARY ALGORITHMS

Evolutionary algorithms [9] are a class of stochastic optimization algorithms whose use in design optimization problems is well established by now [10].

These algorithms are inspired by principles of evolutionary biology and make use of a population of individuals – each individual representing a specific design – to search the design space for the optimum solution. Typical operators applied during evolutionary optimization are selection to direct the search to promising regions of the search space, recombination to combine promising features of known solutions, and mutation to introduce some random changes of the solutions.

In our approach to 3D turbine blade optimization, we use a special variant of evolutionary algorithms namely an evolution strategy (ES) with covariance matrix adaptation (CMA) [11]. The basic idea of CMA-ES is to make maximum use of the information contained in the search history for a self-adaptation of the search direction that is defined in terms of the covariance matrix of a normal distribution from which new tentative solutions or individuals are drawn. Thereby the population size is decoupled from the dimension of the search space.

Especially the latter feature is indispensable in 3D blade optimization which is characterized by a fundamental conflict: on the one hand the design space is very high-dimensional. As a consequence a large number of different designs has to be evaluated during optimization. On the other hand each evaluation of the blade performance is a computationally extremely demanding task so that only a limited number of evaluations can be afforded.

Blade Model

A crucial point in design optimization is the parametric model of the geometry that will be optimized since this determines the design space, i. e. the set of all possible designs and the topology of the design or quality space.

There are a number of requirements for the parametric model:

- flexibility: the model must be flexible enough to represent wide variety of different designs,
- compactness: the number of parameters describing the model must be low enough to allow for reasonable conver-
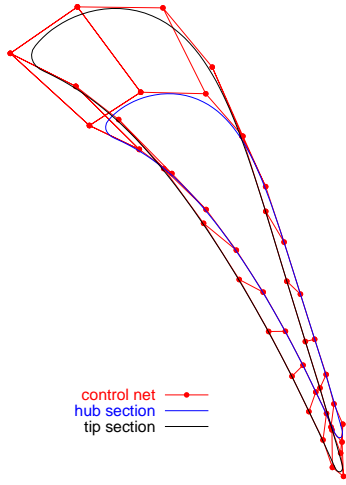
Copyright © 2005 by ASME

Figure 4. The blade model is created from the hub section (blue) and the tip section (black) of the baseline blade. These sections are defined by 25 control points each. The control net of the baseline surface model, that connects neighboring control points is depicted by a red line.

gence times of the optimization algorithm, and

- locality: variations of a single model parameter should result in only local variations of the model and should not affect the global model shape.

A good choice to fulfill these requirements is to use non-uniform rational B-spline (NURBS) surfaces [12] to represent the blade. A B-spline surface is a tensor product of two B-spline curves and hence is defined by two parameters, a set of control points and two knot vectors. Usually not all of these parameters are subject to optimization. We should note that the NURBS representation only fulfills the flexibility condition if the number of control points is sufficiently large.

Our blade model consists of a B-spline surface defined by a periodically closed cubic B-spline in one parameter direction and a second order open B-spline in the other direction. The hub section and the tip section of the blade are each modeled using 25 control points so that all in all 50 control points are used. The control net of the blade model is shown in Fig. 4. Using the co-ordinates of these 50 three-dimensional control points directly as design variables would result in a 150-dimensional search space. Fortunately, we can exploit two facts to reduce the search space dimension to only 88:

1. We note that we use closed periodic splines in the first parameter direction of the blade surface model to achieve a closed and seamless shape that has no beginning or end points. This implies that the first d and the last d control points of each blade section coincide. Here d denotes the degree of the splines which is $d = 3$ in our case of cubic splines. This means that each of the two blade sections is

defined by only $25 - 3 = 22$ independent control points.

2. The hub section as well as the tip section of the blade are defined to lie on cylindrical surfaces. This means the z-coordinates of the control points are implicitly fixed by the blade geometry. Hence we only need to consider the x- and y-coordinates of the control points. This means we have $2 \times 22 = 44$ parameters for each section. In total this makes $2 \times 44 = 88$ design parameters.

The knot vectors are not subject to optimization. Also the end-wall geometry is fixed. Hence it is only the blade geometry that is subject to optimization. Our design parameters – the x- and y-coordinates of the non-periodic control points – are completely free to move. There are no constraints imposed on their location.

Objective Functions

The performance of a specific blade design was given by a weighted sum of the two objectives of the total mass averaged pressure loss and the maximum variation of the pitch-wise static outlet pressure. The averaged pressure loss is estimated far downstream at station 3 for considering mixing losses (see Fig. 3) and the variation of the outlet static pressure is estimated at station 2, just downstream of the TE, cf. Fig. 3. Minimization of these aggregated objectives was subject to a number of constraints as detailed below:

$$f = w_1 t_1 + w_2 t_2 + \sum_{i=3}^{6} w_i t_i^2 \to \min \qquad (1)$$

with

t_1	ω
t_2	PST_{VAR}, cf. Eq. 2
t_3	$\max(0, |\beta_{2,design} - \beta_2| - \delta\beta_2)$
t_4	$\max(0, \Theta_{min,design} - \Theta_{min})$
t_5	$\max(0, \Theta_{TE,min,design} - \Theta_{TE,min})$
t_6	$\max(0, s_{max} - s_{max,design})$

We used the following design values and tolerances:

$\beta_{2,design}$	72.0 deg
$\delta\beta_2$	0.5 deg
$\Theta_{min,design}$	0.72 mm
$\Theta_{TE,min,design}$	0.9 mm
$s_{max,design}$	0.706

We considered two variants of the objective function Eq. 1: (*i*) $w_2 = 0$, i.e., only the pressure loss ω was minimized, and (*ii*) $w_1 t_1 \approx w_2 t_2$, i.e., the pressure loss ω and and an additional criterion, the pitch-wise variation of the static outlet pressure

PST_{VAR}, are jointly minimized where PST_{VAR} is defined as

$$PST_{VAR} = \max_{i=1...K} \left(\left| \max_{j=1...L} \{PST(i,j)\} - \min_{j=1...L} \{PST(i,j)\} \right| \right) . \tag{2}$$

Initially both objectives received the same weight.

The initial blade model lies within the feasible region of the design space. According to Eq. 1 only violated constraints contribute to the objective function. The weights on the constraints were chosen such that the contribution of a violated constraint by far outweighs the contribution of the objectives in order to quickly drive the search back into the feasible region.

Flow Solver

For the simulation of the fluid dynamic properties of the blade designs we used the parallelized 3D in-house Navier-Stokes flow solver HSTAR3D, see [13], with Wilcox's k-ω two equations model [14]. In order to obtain a high resolution of the boundary layer development, CFD calculations for the baseline blade have been performed prior to optimizations for determining the grid size. The computational grid consisted of $175 \times 52 \times 64 = 582,400$ cells. The average y^+ of the first grid point from the wall is about 1.5 for all calculations. The computation time for one run with this grid depends on the blade geometry and varies between 2.5 hours and 6 hours on an AMD Opteron 2 GHz dual processor.

Optimization Algorithm

A flow-chart of our optimization environment is given in Fig. 5. The basic set-up is governed by two parallelization levels. On the first level the evolutionary operators are used to generate the offspring population, i.e., the new blade designs. In our algorithm, we do not use a recombination procedure. Instead changes are induced during mutation by adding normally distributed random numbers to the design parameters that are subject to optimization. As noted in the introduction, the covariance matrix of the normal distribution is adapted to the local topology of the search space. The λ offspring individuals – here λ denotes the offspring population size – are evaluated in parallel by sending each blade representation to separate slave processes using the Parallel Virtual Machine (PVM) library [15]. The slave processes generate the computational grid and run the flow-solver using an additional set of four processes which are distributed using MPI [16]. This constitutes the second level of parallelization. The slave processes calculate the objective function Eq. 1 and send the resulting quality value back to the master process. The master collects the quality values for all λ individuals or blade designs. Next, the best μ designs are selected from these λ individuals to become the parent population of the next generation. In evolutionary algorithms this type of "deterministic" selection method is written as (μ,λ)-selection. The evolutionary
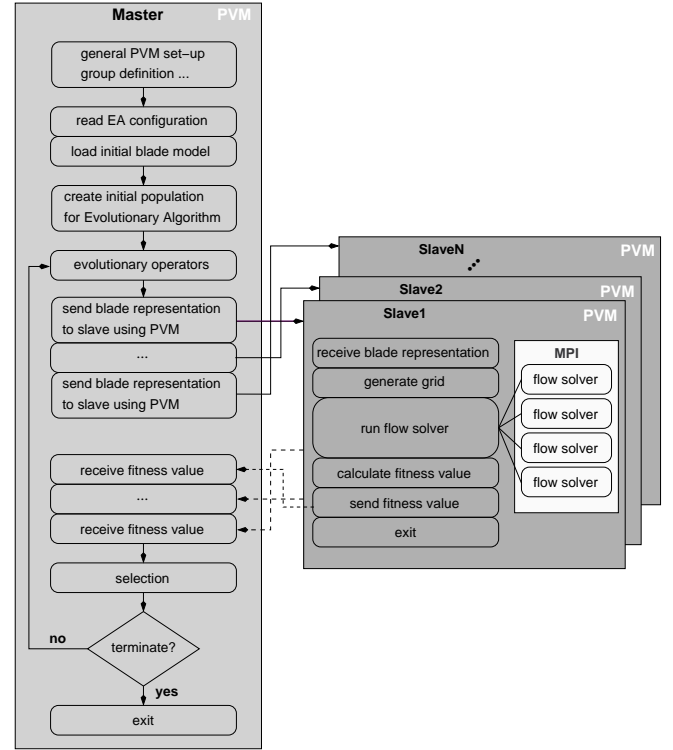

Figure 5. Program flow chart. The program is parallelized at 2 levels: the first level of parallelization is a master-slave model that uses PVM [15] to organize the distribution of single individuals to slave processes while the second level that is started by the slave processes is a node-only model for parallelizing the flow solver calculations using MPI [16].

cycle proceeds with the creation of the next offspring generation as long as the stop criteria are not met. Ideally, stop criteria should depend on the expected performance gain and stop the optimization when this value falls below a certain threshold. In reality, the optimization is stopped because of time constraints.

For the results presented in this paper, a (μ, λ) CMA-ES with $\mu = 1$ parent individual and $\lambda = 10$ offspring individuals was used. The optimization was initialized with a geometry similar to the baseline blade. All offspring individuals were evaluated in parallel. For this we used a 40 processor computing cluster: 10 parallel processes were running in the first level of parallelization and each of these spawned 4 processes in the second level of parallelization. The results shown here were obtained after about one month of computation time.

RESULTS AND DISCUSSION

In Fig. 6 we show the value of the objective function or fitness function during optimization. The vertical lines in this figure indicate that in some cases even the fitness of the best individual of the population lies outside of the range of the plot. This
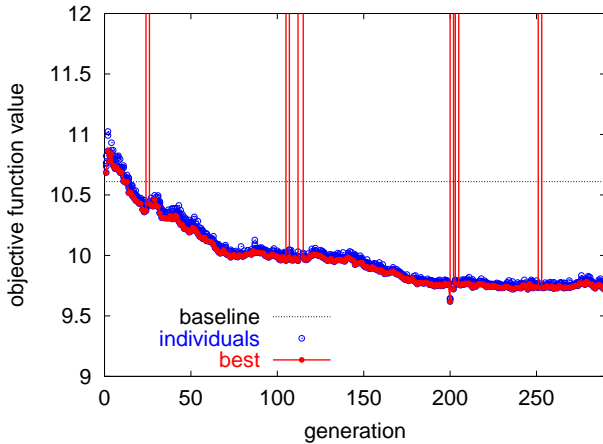
Figure 6. The objective function values during optimization. The single individuals are marked by open circles (blue), the best individual of each generation (red) are connected. The baseline blade performance is indicated by a dotted line. The vertical lines in the plot denote cases in which even the best individual of the population does not comply with the constraints and hence receives a high penalty.

means that the complete population moved out of the feasible region of the optimization problem. In principle, this is critical because the population may be lead astray and not be driven back into the feasible region thus causing a failure of the optimization process. But here these outliers are smoothly absorbed by the optimizer and do not disturb the process. This demonstrates the stability of the optimization method.

The optimized blade geometries at the hub and tip sections are shown in Fig. 7 (a) and (b) together with the baseline sections. In the hub section of the optimized blade, the curvature of the frontal part on the suction surface is considerably reduced and a bent part near the TE can be seen, see Fig. 8. It seems that the loading pattern at the hub is significantly shifted toward downstream. This tendency is also observed for the tip section.

Figure 9 shows a comparison of the radial distribution of the total pressure loss coefficient at station 2 and station 3 for the baseline and the optimized blade. The data were obtained from a 3-D CFD analysis. In station 2, it can be seen that the total pressure loss near the hub end-wall for the optimized blade is lower as compared to the loss of the baseline blade. This tendency is still present in station 3, although there is a strong development of the boundary layer due to the high-swirling flow. Fig. 10 shows the Mach number characteristics for the hub section for both blades, obtained from a 2-D CFD analysis. As expected, the performance of the optimized blade is apparently worse than that of the baseline blade. On the other hand, as already shown in Fig. 9, the optimized blade is better than the baseline blade. This means that the inward-radial cross flow on the blade suction surface of the optimized blade is significantly suppressed. For
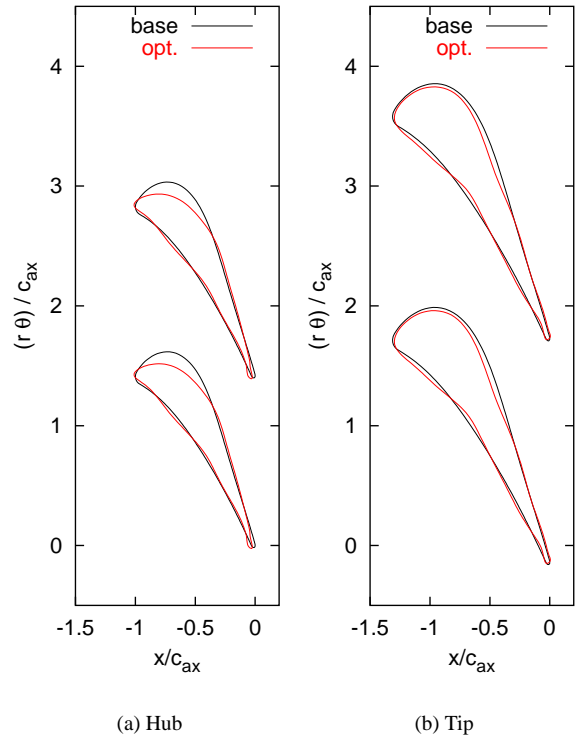

(a) Hub   (b) Tip

Figure 7. Comparison of blade geometries for (a) the hub section and (b) the tip section of baseline blade (blue) and optimized blade (red), resp.
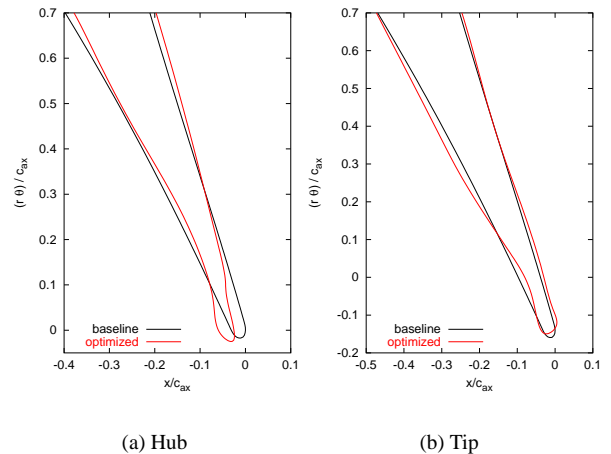

(a) Hub   (b) Tip

Figure 8. Comparison of the TE parts of the blade geometries for (a) the hub section and (b) the tip section of baseline blade (blue) and optimized blade (red), resp.
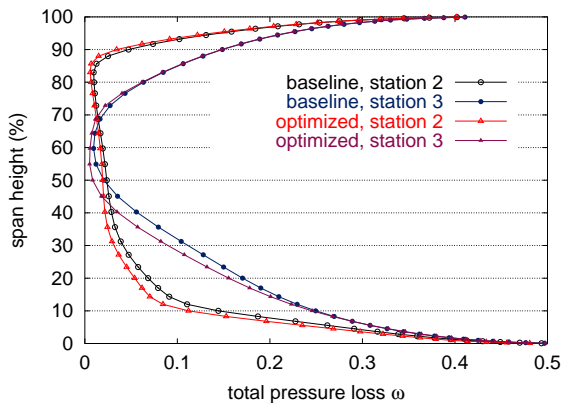
Figure 9. Comparison of radial total pressure loss distribution at station 2 and station 3 for baseline (black/blue) and optimized (red/dark red) blade.
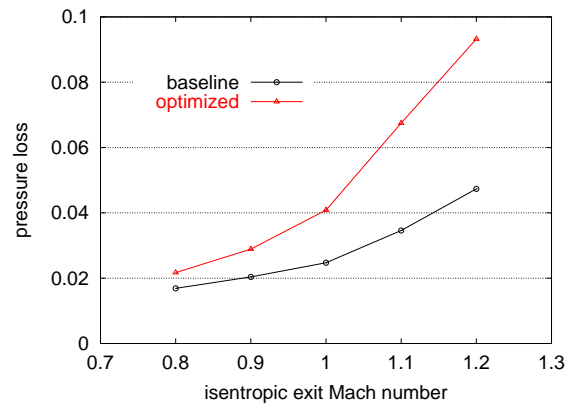

Figure 10. Comparison of the Mach number characteristics of baseline (black) and optimized (red) blade.
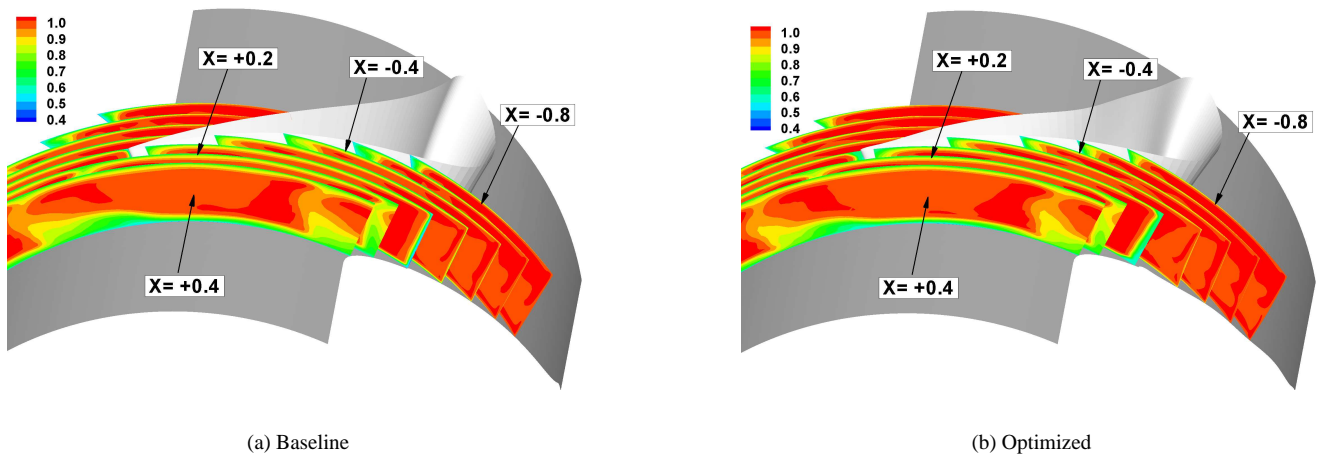

(a) Baseline

(b) Optimized

Figure 11. Positions of blade to blade cross-sections for (a) the baseline blade and (b) the optimized blade. The cross sections were taken at $X = -0.8$, $X = -0.6, X = -0.4, X = -0.2, X = 0.0, X = 0.2, X = 0.4$, see Fig. 3.

further analysis, some cross-sectional blade to blade views are numerically investigated.

The locations of the cross-sections at each axial chord are shown in Fig. 11, cf. Fig. 3. The contours indicate the total pressure. It can be seen that the flow pattern at $X = +0.4$ for the optimized blade is better than the one for the baseline blade. Figure 12 shows the details of the contours at $X = -0.8$, -0.4 and +0.2 (around station 2).

Overall, the total pressure pattern is very similar for both blades. However, there is a big difference between both blades in the boundary layer development on the blade suction side. At $X = -0.8$, corresponding to about mid-axial chord position (50%), the flow pattern is already different between both blades. The boundary layer of the optimized blade is slightly thinner than

that of the baseline blade and the boundary layer on the tip-side is thicker than that on the hub-side. It seems that the inward-cross flow in the optimized blade is significantly suppressed. At $X = -0.4$, corresponding to about 75% of axial chord position, we can see the large difference in the boundary layer development between both blades. Just downstream of the stator, i.e., around a rotor LE position of $X = +0.2$, the performance of the optimized blade is still better than that of the baseline blade, although the difference is reduced. The cause for the reduction of the difference downstream of the TE seems to be due to a sudden decrease of velocity around 85-95% of axial chord and a stronger TE shock on the pressure side for the optimized blade, see Fig. 13 (a) and (b).

Figure 13 shows the blade surface isentropic Mach number

7

(a) Baseline, $X = -0.8$ (b) Optimized, $X = -0.8$

(c) Baseline, $X = -0.4$ (d) Optimized, $X = -0.4$

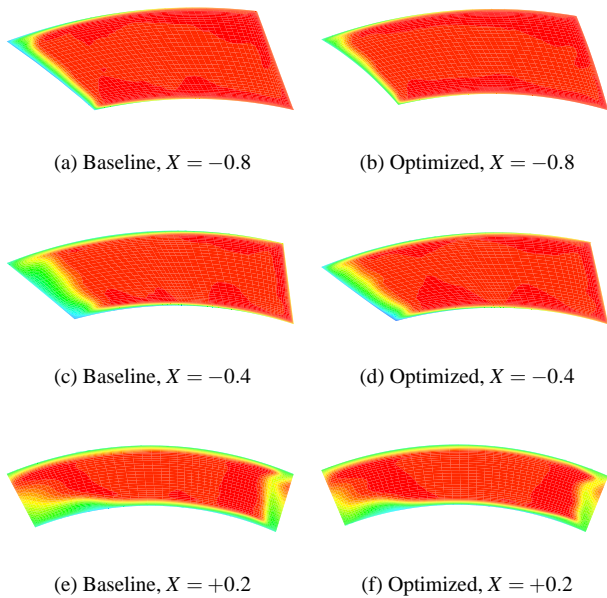(e) Baseline, $X = +0.2$ (f) Optimized, $X = +0.2$

Figure 12. Comparison of total pressure contours at the stream-wise positions of $X = -0.8$, $X = -0.4$, and $X = +0.2$ (from top to bottom) for the baseline blade (left) and the optimized blade (right). In each contour plot, the left edge is on the suction side while the right edge is on the pressure side, cf. Fig. 11.

for the baseline and the optimized blade. As previously mentioned, the loading pattern of the optimized blade is significantly shifted downstream. Particularly noticeable is the steep increase of the velocity near the TE on the pressure side. This is due to the bent part of the blade geometry near the TE. Also, it seems that the trailing edge shocks on the pressure side and on the suction side of the optimized blade are slightly increased as compared to the baseline blade. This might also affect the pitch-wise static pressure variation of the optimized blade downstream of the trailing edge.

The properties mentioned above are particularly visible in Fig. 14, where the isentropic Mach number distribution at 10% of spanheight – near the hub region – is shown for the baseline blade and the optimized blade. Close to the the mid-axial chord position, the pitch-wise static pressure gradient is reduced in the optimized blade, while the gradient near the TE is increased. These features seem to control the pitch-wise migration of the low momentum fluid near the tip casing, as well as near the hub endwall. Figure 15 shows the iso-surface of entropy around the hub region for the baseline and optimized blade. The entropy production near the casing wall is omitted in order to obtain a better view of the iso-pattern. The same threshold of the iso-surface is used for both blades. It can be seen that the entropy production of the optimized blade is delayed downstream and that the corner-separation region, observed in the baseline near SS around TE,
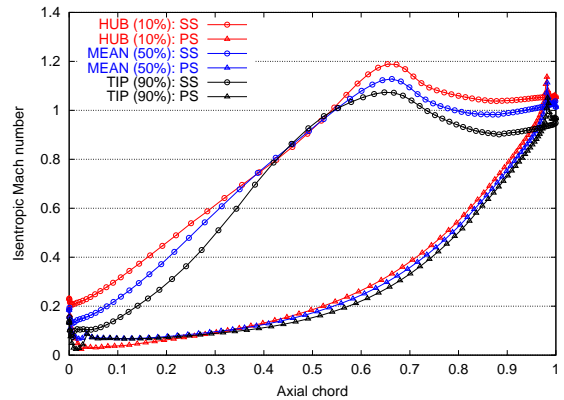
(a) Baseline
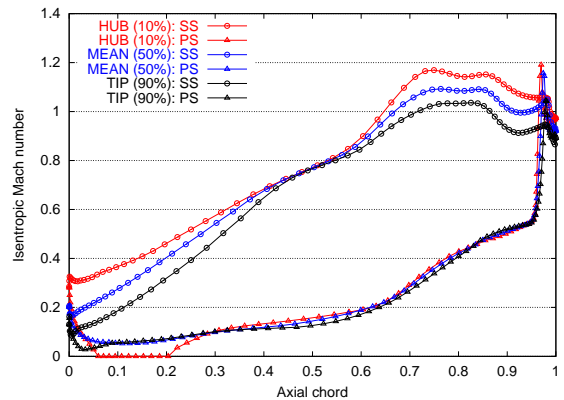
(b) Optimized

Figure 13. Blade surface isentropic Mach number distribution for (a) the baseline blade and (b) the optimized blade. In both cases the LE is located at axial chord length $c_{ax} = 0.0$ and the TE is located at $c_{ax} = 1.0$. The figures show the Mach number distributions at 10% span-height (red), 50% span-height (blue), and 90% span-height.

is significantly diminished in the optimized blade. Fig. 16 shows the entropy production accumulated from 0% to 50% spanheight at each axial chord position within blade to blade. The entropy production of the optimized blade is smaller than that of the baseline blade from the downstream position of $X = -1.0$, that is, from about 44% axial chord position. Also, the maximum gain is obtained around 66% of axial chord position ($X = -0.6$). Fig.17 shows the comparison of the "blade surface streamline pattern" and "the static pressure contours" for the baseline and optimized blade. It can be seen that the strong inward-cross flow, starting at around mid-chord position for the baseline, is significantly suppressed for the optimized one. Therefore, we can see that due to
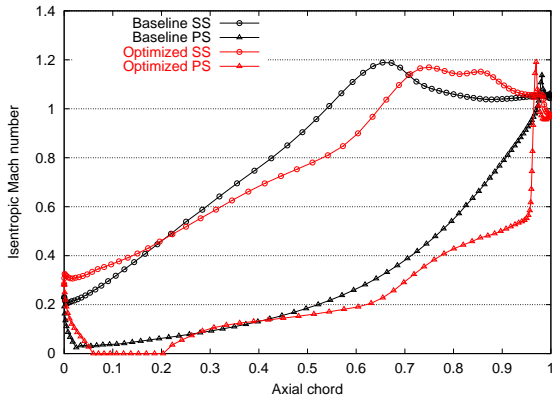
8

Figure 14. Comparison of blade surface Mach number at 10% span-height for the baseline blade (black) and the optimized blade (red).

the pitch-wise weaker driving force around the mid axial chord position the strong inward radial cross flow on the suction surface observed in the baseline blade is weakened and/or shifted more downstream in the optimized blade.

Figure 18 (a) and (b) show contours of the static pressure distribution at 10% spanheight for the baseline and the optimized blade, respectively. Fig. 19 shows a comparison of the pitch-wise static pressure variation at 10% spanheight at station 2 (downstream rotor LE position).

We observe from Figs. 18 and 19 that there is a relatively small pitch-wise variation of the static pressure for the baseline blade. This pattern is very similar to the one published by Vascellari et al. [17] (Fig. 2 in their paper), although the variation level (about 0.48 to 0.52) for the baseline blade is smaller than in Vascellari's paper (about 0.4 to 0.5). However, we observe a considerably larger variation (about 0.46 to 0.54) for the optimized blade due to the extreme aft-loaded pattern. The variation level for the optimized blade presented here is much closer to the one of Vascellari's original blade.

Besides reducing the pressure loss, it is generally also desirable to minimize the pitch-wise pressure variation. Whether a "keep below a certain threshold" strategy is in practical terms more advisable than true minimization will be discussed in the next section. Strong pitch-wise variation is not desirable, since unsteady losses might occur from the interaction between stator and rotor. Therefore, we started a second optimization where we combined (aggregated) the pressure loss and the pressure variation criteria.

In Fig. 19 the additional optimization result is shown denoted as *optimized-II*. A very small variation of the pitch-wise static pressure distribution is clearly observed as compared to the baseline blade.

However, unfortunately, the total pressure loss is worse than for the baseline, as shown in Fig. 20. So far, we have not been able to simultaneously minimize total pressure loss and pitch-

(a) Baseline

(b) Optimized

Figure 15. Comparison of iso-surface of entropy for (a) the baseline blade and (b) the optimized blade.
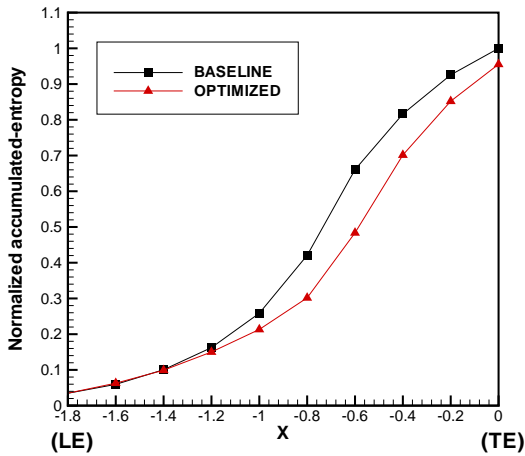
Figure 16. Comparison of normalized accumulated-entropy within the blade passage for the baseline blade (black) and the optimized blade (red).

wise static pressure variation. In the next section, we will discuss how to deal with this trade-off between both criteria from an optimization point of view.

CONCLUSION

In this study, we employed a numerical, stochastic optimization method, namely evolution strategies, to design an ultra-low-AR transonic turbine stator blade. The target was to identify new aerodynamic design concepts that achieve low aerodynamic losses and low pressure variations. From an aerodynamic point of view, we can draw the following conclusions:

- The extreme-aft loaded blade that is a result of a noticeable bent part near the TE is effective for reducing secondary losses.
- The reduction of the secondary flow loss is a result of the reduction of the pitch-wise driving force which leads to a reduced migration of low momentum fluid near the tip and/or hub casing around the mid-axial chord position.
- This results in a considerably delayed development of the boundary layer on the suction surface.
- It seems difficult to resolve the trade-off relation between aerodynamic performance and variation of pitch-wise static pressure distribution. This issue will be one of the major subjects of our future work.

The optimization results that we presented in this work, are not the converged solutions of the evolution strategy. Indeed it is difficult to estimate both convergence and expected future progress. However, one can use several heuristics to stop the op-
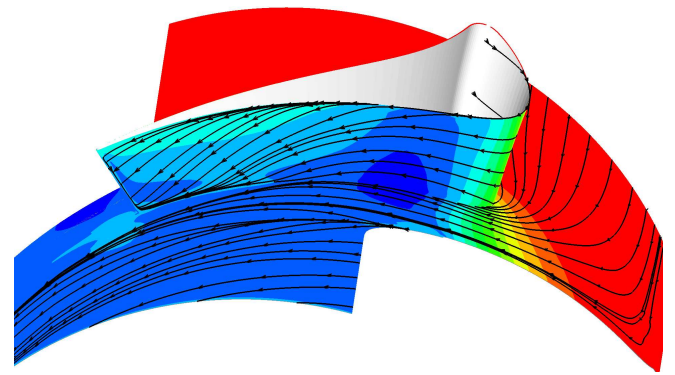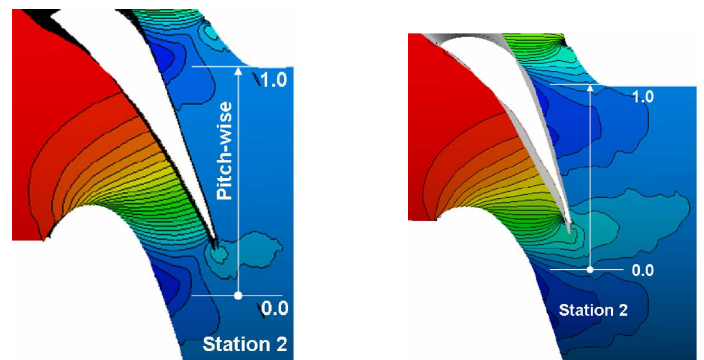

(a) Baseline
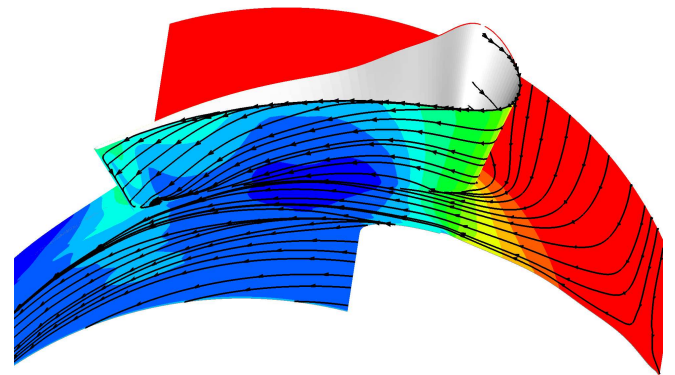
(b) Optimized

Figure 17. Comparison of "blade surface streamline pattern" and "static pressure contours" for (a) the baseline blade and (b) the optimized blade.

(a) Baseline   (b) Optimized

Figure 18. Contours of static pressure distribution at 10% spanheight for (a) the baseline blade and (b) the optimized blade.
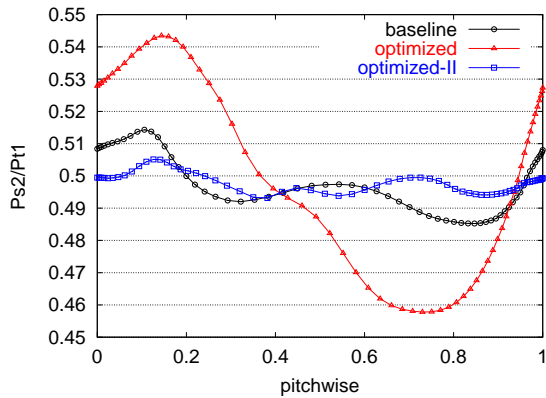
Figure 19. Pitch-wise static pressure distribution at 10% span height for the baseline blade (black), the optimized blade (red), and the second optimized blade (blue).
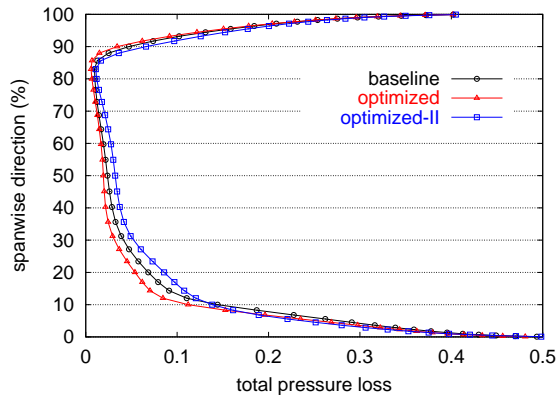

Figure 20. Span-wise total pressure distribution at station 2 for the baseline blade (black), the optimized blade (red), and the aggregated optimized blade (blue).

timization process, among those are small diversity in the solutions during recent generations, sufficient improvement reached, and allocated computation time exceeded.

From the optimization point of view the combination of the different criteria and constraints constitutes an interesting problem. In particular the relation between the pressure loss and the variation of the static outlet pressure deserves further attention. The trade-off relation between both objectives has been previously pointed out in the literature [18]. In this paper, we employed the simplest way to combine the two objectives, namely linear aggregation. Its advantage is that the problem remains single objective and more efficient algorithms can be used than are available for multi-objective optimization. The drawback is (besides the linearity of the combination) the ad-hoc choice of the relative weights. Indeed as our results show, the static pressure variation has received too much attention during the optimiza-

tion. In other words, the selection pressure toward smaller pressure loss values was not sufficient. There are two principle ways to proceed. First, we can avoid the combination of both objectives and use multi-objective optimization methods [19, 20] to determine the Pareto, i.e., the trade-off, curve. Second, we can regard the second criterion as a constraint. Thus, we set the variation of the static outlet pressure of the baseline blade as a soft constraint, so that slight overshooting is penalized only slightly, and only optimize the pressure loss. We intend to follow both pathways in future optimizations.

Another topic for future research is the representation of the blade model. In this study, we used a B-spline surface representation. However, the number of control points necessary to achieve sufficient flexibility with this kind of model may become infeasibly large since this number directly determines the dimension of the search space and hence the convergence time of the optimization algorithm. This trade-off between the flexibility of the model and the search space dimension cannot be resolved easily if the representation is static. Instead, a dynamic and adaptive representation is required as proposed in [21].

REFERENCES

[1] Williamson, R. G., Moustapha, S. H., and Huot, J. P., 1986. "The effect of a downstream rotor on the measured performance of a transonic turbine nozzle". ASME 86-GT-103.

[2] Dunham, J., and Came, P., 1970. "Improvements to the Ainley-Mathieson method of turbine performance". ASME 70-GT-02.

[3] Kacher, S. C., and Okapuu, U., 1981. "A mean line prediction method for axial turbine efficiency". ASME 81-GT-58.

[4] Moustapha, S. H., Kacker, S. C., and Tremblay, B., 1989. "An improved incidence losses prediction method for turbine airfoils". ASME 89-GT-284.

[5] Kuno, N., and Sonoda, T., 2004. "Flow characteristics in a transonic ultra-low-aspect-ratio axial turbine vane". *Journal of Propulsion and Power,* **20** (4) , pp. 596–603.

[6] Sonoda, T., Arima, T., Olhofer, M., Sendhoff, B., Kost, F., and Giess, P., 2004. "A study of advanced high loaded transonic turbine airfoils". ASME Paper No. GT 2004-53773.

[7] Arnone, A., Bonaiuti, D., Focacci, A., Pacciani, R., Greco, A., and Spano, E., 2004. "Parametric optimization of a high-lift turbine vane". ASME Paper No. GT 2004-54308.

[8] Kaemmerer, S., Mayer, J., Paffrath, M., Wever, U., and Jung, A., 2003. "Three-dimensional optimization of turbomachinery bladings using sensitivity analysis". ASME Paper No. GT 2003-38037.

[9] Bäck, T., Fogel, D. B., and Michalewicz, T., Eds., 2000. *Evolutionary Computation 1: Basic Algorithms and Operators*. Institute of Physics.

[10] Osyczka, A., 2002. *Evolutionary Algorithms For Single And Multicriteria Design Optmization*. Physica-Verlag.

[11] Hansen, N., and Ostermeier, A., 2001. "Completely de-randomized self-adaptation in evolution strategies". *Evolutionary Computation,* **9** (2) , pp. 159–195.

[12] Farin, G., 1997. *Curves and Surfaces for Computer-Aided Geometric Design*, 4th ed. Academic Press, San Diego.

[13] Arima, T., Sonoda, T., Shirotori, M., Tamura, A., and Kikuchi, K., 1999. "A numerical investigation of transonic axial compressor rotor flow using a low-Reynolds-number $k - \varepsilon$ turbulence model". *ASME Journal of Turbomachinery,* **121** (1) , pp. 44–58.

[14] Wilcox, D. C., 1988. "Reassessment of the scale-determining equation for advanced turbulence models". *AIAA Journal,* **26** , pp. 1299–1310.

[15] Geist, A., Beguelin, A., Dongarra, J., Jiang, W., Mancheck, R., and Sunderam, V., 1994. *PVM: Parallel Virtual Machine: A Users' Guide and Tutorial for Network Parallel Computing*. MIT Press.

[16] "MPI: A message-passing interface standard", http://www-unix.mcs.anl.gov/mpi/.

[17] Vascellari, M., Denos, R., and Van den Braembussche, R. A., 2004. "Design of a transonic high-pressure turbine stage 2D section with reduced rotor/stator interaction". ASME GT2004-53520.

[18] Shelton, M. L., Gregory, B. A., Lamson, S. H., Moses, H. L., Doughty, R. L., and Kiss, T., 1993. "Optimization of a transonic turbine airfoil using artificial intelligence, CFD and cascade testing". ASME Paper 93-GT-161.

[19] Okabe, T., Jin, Y., and Sendhoff, B., 2003. "Evolutionary multi-objective optimization with a hybrid representation". In Congress on Evolutionary Computation (CEC), vol. 4, IEEE Press, pp. 2262–2269.

[20] Sonoda, T., Yamaguchi, Y., Arima, T., Olhofer, M., Sendhoff, B., and Schreiber, H.-A., 2004. "Advanced high turning compressor airfoils for low Reynolds number condition, Part 1: Design and optimization". *Journal of Turbomachinery,* **126** (3) , pp. 350–359.

[21] Olhofer, M., Jin, Y., and Sendhoff, B., 2001. "Adaptive encoding for aerodynamic shape optimization using evolution strategies". In Congress on Evolutionary Computation (CEC), IEEE Press, pp. 576–583.